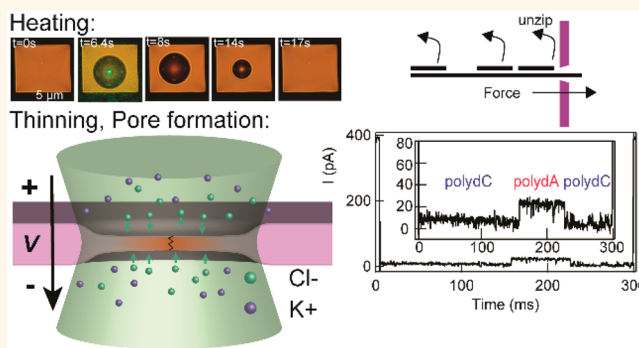


Photothermally Assisted Thinning of Silicon Nitride Membranes for Ultrathin Asymmetric Nanopores

Hirohito Yamazaki,[†] Rui Hu,[‡] Qing Zhao,[†] and Meni Wanunu^{*,†}[†]Department of Physics, Northeastern University, Boston, Massachusetts 02115, United States[‡]State Key Laboratory for Mesoscopic Physics, School of Physics, Peking University, Beijing 100871, People's Republic of China**S** Supporting Information

ABSTRACT: Sculpting solid-state materials at the nanoscale is an important step in the manufacturing of numerous types of sensor devices, in particular solid-state nanopore sensors. Here we present mechanistic insight into laser-induced thinning of low-stress silicon nitride (SiN_x) membranes and films. In a recent study, we observed that focusing a visible wavelength laser beam on a SiN_x membrane results in efficient localized heating, and we used this effect to control temperature at a solid-state nanopore sensor. A side-effect of the observed heating was that the pores expand/degrade under prolonged high-power illumination, prompting us to study the mechanism of this etching process. We find that SiN_x can be etched under exposure to light of $\sim 10^7$ W/cm^2 average intensity, with etch rates that are influenced by the supporting electrolyte. Combining this controlled etching with dielectric breakdown, an electrokinetic process for making pores, nanopores of arbitrary dimensions as small as 1–2 nm in diameter and thickness can easily be fabricated. Evidence gathered from biomolecule-pore interactions suggests that the pore geometries obtained using this method are more funnel-like, rather than hourglass-shaped. Refined control over pore dimensions can expand the range of applications of solid-state nanopores, for example, biopolymer sequencing and detection of specific biomarkers.

KEYWORDS: nanopores, photothermal heating, nanofabrication, dielectric breakdown, single-molecule



Methods to shape materials at the nanoscale have received much attention in recent years, largely due to the need for technologies that allow the investigation of quantum phenomena at the nanoscale, but also as vehicles for interfacing with the molecular/biomolecular world. Nanopore sensors are prime examples of nanoscale devices that sense small molecules, biomolecules, and their complexes. Sensing in nanopores is most frequently performed by applying a voltage across a nanopore that contains two electrolyte baths across it and measuring as a function of time the flux of ions that cross the pore. When an analyte (e.g., DNA, protein, or a small molecule) occupies the pore, the ion flux temporarily changes, affording indirect electrical detection of biomolecules in a label-free manner.

An attractive form of nanopores for future integration into sensing devices is a silicon chip that contains a freestanding membrane composed of silicon nitride (SiN_x) or another material, through which a hole is fabricated using one of various methods. Nanopore sensors are not “one-size-fits-all”; their dimension requirements are typically commensurate with

the analyte size. Therefore, the nanopore physical properties, which include its diameter, length, shape, and interfacial properties, typically need tailoring for optimal sensing. A variety of approaches have been developed for nanopore fabrication, which range from chemical etching to electron-^{1–3} and ion-^{4,5} beam irradiation. Nanopores in two-dimensional (2D) materials have also gained attention due to their atomically thin and well-defined pore shape, which in principle should confer high resolution for biopolymer analysis.^{6–11} Recently, a method called dielectric breakdown was pioneered by the Tabard-Cossa group,^{12–15} in which applied voltage across a thin membrane immersed in electrolyte induces stochastic breakdown of the membrane material, resulting in the creation of a path through which ions can traverse the membrane. Following nanopore formation, the nanopore shape is “conditioned” by applying voltage across the newly

Received: September 5, 2018

Accepted: November 20, 2018

Published: November 20, 2018

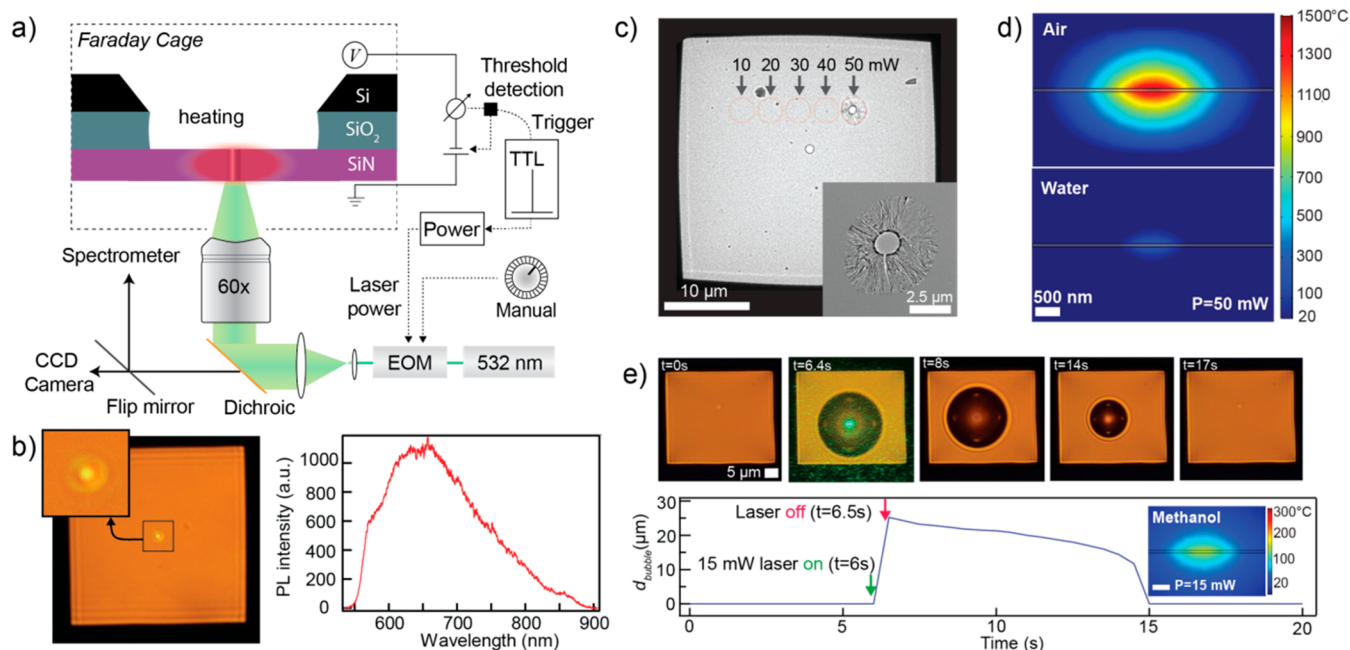


Figure 1. Photothermal effect on a SiN_x membrane. (a) Collimated 532 nm laser beam is focused on a SiN_x membrane using a 60x inverted objective. SiN_x membrane is mounted between two fluidic chambers (top is *cis*, bottom is *trans*). Laser power is electrically controlled using an electro-optics modulator. The current across a pore is monitored by applying bias between Ag/AgCl electrodes (voltage applied to *cis* chamber in scheme). Reflected 532 nm laser, transmitted lamp light, and fluorescence after passing through dichroic mirror are detected by CCD camera or spectrometer. (b) Left: Optical image of $40 \mu\text{m} \times 40 \mu\text{m}$ 75 nm thick- SiN_x membrane on which a 532 nm laser beam is focused. Zoomed-in portion shows airy rings around the focused beam. Right: PL spectrum of the 75 nm-thick SiN_x membrane excited by a 47 mW laser beam for 1 s. (c) TEM image of 75 nm-thick- SiN_x membrane following 3–5 s illumination of 10, 20, 30, 40, and 50 mW in air. Inset: TEM image of the resulting SiN_x membrane ablation by the 50 mW laser spot. (d) 2D finite-element COMSOL simulation of the steady-state temperature distribution around a 50 mW laser-irradiated air-immersed (top) and water-immersed (bottom) SiN_x membrane. (e) Microbubble nucleation on a 75 nm-thick SiN_x membrane immersed in methanol. Top: Series of optical images obtained during the bubble nucleation cycle, in which a 75 nm-thick membrane surrounded by methanol is illuminated using a 15 mW laser spot on the membrane at 6 s, and laser was turned off at 6.5 s (image series obtained from [Movie M1](#), see Supporting Information). Bottom: Bubble diameter (d_{bubble}) vs time. Bottom Inset: 2D finite-element simulation of the temperature distribution (scale bar = 400 nm).

formed pore, which forms a pore that is suitable for sensing experiments. This method has gained popularity^{16–19} because the pores can be fabricated following assembly in a fluidic cell, and the fabricated pores are typically fully hydrated, so no aggressive chemical cleaning steps are required postfabrication to promote hydrophilicity. Methods to control the position of nanopores on the membrane using a combination of local thinning and localized light excitation have been reported,^{20–23} and optical imaging has allowed the visualization of nanopore formation and position.^{24,25}

Finally, machining nanoscale holes has been reported using ultrafast or continuous laser illumination on membranes composed of amorphous^{21,26–28} and 2D materials.^{11,29} The mechanism of laser fabricated nanoscale holes depends on the substrate material as well as the buffer conditions. For example, in the case of WS_2 membranes, light absorption likely leads to photo-oxidation of the material by (1) reaction with water or oxygen, then replacement or dislocation of sulfur atoms, or (2) defect nucleation followed by reaction with oxygen, which lead to pores generated in water.^{11,29} For amorphous SiN_x , a several-mW intensity visible laser has been used to etch the membrane down to the formation of a pore, and this was shown to be a function of laser power and wavelength.²¹ The proposed SiN_x etching mechanism was a photochemical reaction associated with water, which is not temperature activated, and using this photochemical etching at a laser line of 488 nm, Gilboa *et al.* obtained controllable hourglass-shaped

pores, indicated by monitoring the transmembrane current using a weak probing voltage (~ 300 mV).²¹

Here, we investigate in detail the factors that lead to light-induced etching of SiN_x , focusing on photoexcitation, heating, and chemical catalysis as the driving factors. First, we show that high temperatures can be obtained at the pore under laser irradiation, depending on the surrounding environment and the laser power. We then show that coating of the SiN_x with a conformal layer of HfO_2 effectively eliminates etching under illumination, suggesting that the solid-electrolyte interface is required for optically induced SiN_x etching. Next, we demonstrate that SiN_x etching rates are affected by the type of salt present in the contacting electrolyte, with chloride being the most effective neutral-pH etch catalyst and hydroxide being a very fast etchant. We find that controlled etching under applied bias and laser/voltage feedback drives the dielectric breakdown of nanopores with small diameters (< 5 nm) and tunable effective thickness (0.5–8 nm). Supported by our observations of asymmetric molecular transport across these nanopores, we conjecture that the pores are asymmetric in shape, exhibiting a funnel-like geometry. This approach can serve as a foundation for high-resolution pores that are comparable in geometry to protein-based nanopores used in DNA sequencing.

Figure 1a shows our laser illumination setup, in which a silicon chip that has a freestanding SiN_x membrane is placed in an inverted microscope (Olympus IX71) and Ag/AgCl

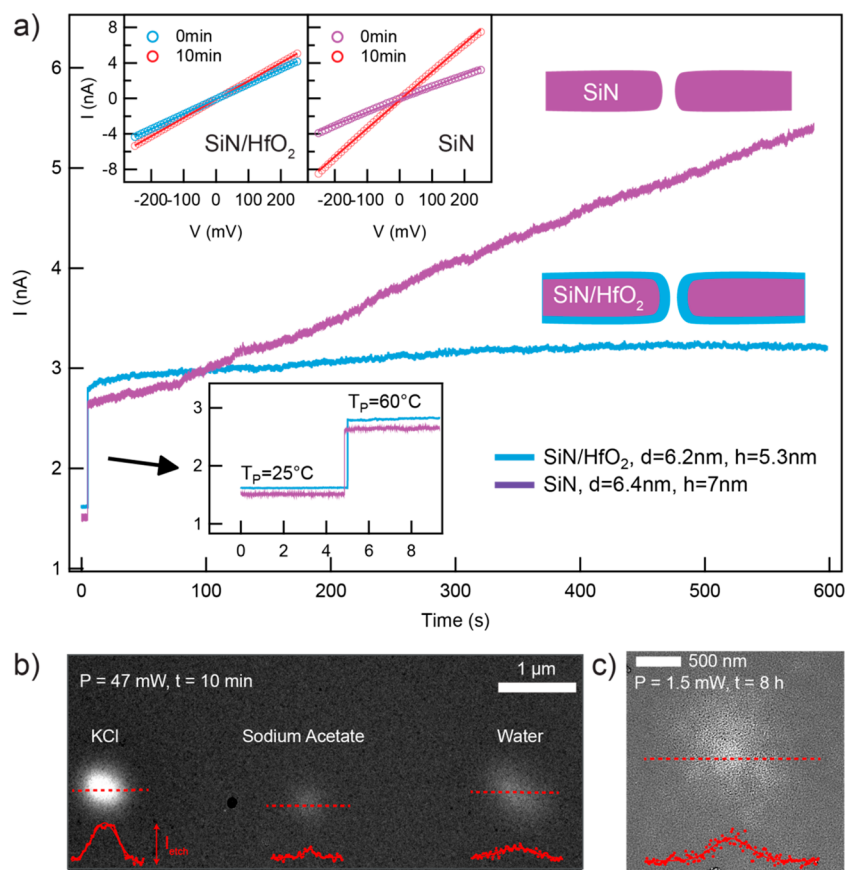


Figure 2. Laser-induced SiN_x etching. (a) Continuous current trace of a SiN_x and HfO₂-coated SiN_x pore at $T_{\text{pore}} = 60^\circ\text{C}$ for 10 min ($V = 100$ mV) under 532 nm laser irradiation (laser turned on after 5 s). Purple line: A 6.4 nm diameter SiN_x pore with 7 nm effective thickness. Blue line: A 6.2 nm diameter of HfO₂-coated SiN_x pore with 5.3 nm effective thickness. Inset top: I - V curves of HfO₂-coated SiN_x and SiN_x pore before and after the 10 min laser illumination. For the HfO₂-coated SiN_x pore, before and after conductance values were 17 nS and 20 nS, respectively. For the SiN_x pore, before and after conductance values were 14 nS and 32 nS, respectively. Expanded current traces at 0–9 s, showing laser turn-on times, are shown in the inset. (b) TEM image of 75 nm-thick SiN_x membrane after 47 mW laser illumination for 10 min in water, 0.4 M sodium acetate, and 0.4 M KCl ($T = 300^\circ\text{C}$). Membrane thicknesses at each point are related to the image brightness, and intensity values for the different buffers were 181, 37, and 49 for KCl, sodium acetate, and water, respectively. (c) TEM image of a 75 nm-thick SiN_x membrane after 1.5 mW laser illumination for 8 h in 4 M KCl.

electrodes across the membrane are used to apply voltage and measure current across the membrane. The membrane is illuminated with a focused laser beam that is expanded and collimated to fill the back plane of the objective (Olympus 60 \times , NA 0.9, air), after passing through an electro-optic modulator (EOM, Conoptics, 302RM) that allows rapid control over the laser power (<10 μs response time). During an experiment, either a probing or a pore-forming voltage is applied, and the measured current across the membrane reports on pore formation. By setting a threshold value for the current, pore formation triggers the laser power to turn off and/or the voltage to be reduced, in order to prevent the rapid expansion of a formed pore. The applied voltage and laser power can also be set manually when not in feedback mode. Reported laser power values throughout this paper were measured after passing through the objective lens (values are not corrected to account for reflection from the coverslip and membrane, 4–7%).

Figure 1b shows a trans-illuminated membrane under laser illumination (note first- and second-order airy rings around the laser spot in inset) as well as a typical photoluminescence (PL) spectrum of the membrane obtained by exciting the membrane using a focused 532 nm laser spot and directing the emission

image to the spectrometer through an optical fiber (QE-Pro, Ocean Optics). The broad SiN_x PL is a result of SiN_x electronic valence-to-conduction band transitions,^{30,31} which ranges throughout the visible to UV region, depending on the local chemical composition in the SiN_x film, in particular, lower values of “ x ” imply lower energy band gaps. Since our SiN_x films are deposited using chemical vapor deposition for the purpose of being low-stress freestanding membranes, our films are Si-rich, with $x \sim 1$ (for stoichiometric SiN_x, $x = 1.33$). Since the PL yield of SiN_x at room temperature is very low ($<10\%$),^{32,33} most of the absorbed light is dissipated nonradiatively, resulting in heating of the surrounding environment. To illustrate this thermal heating effect, in Figure 1c we show a low-magnification TEM image of 75 nm-thick SiN_x membrane after a series of 3–5 s spot exposures at laser powers of 10 mW to 50 mW were made along the membrane in air (dashed red circles shown around each spot position). We found that exciting the membrane at 50 mW creates a 1 μm hole creation within 1 s (see Supporting Movie M1). A close-up TEM image at the site of the hole shows a clear evidence of SiN_x ablation by a rapid heating mechanism, with thermal stress patterns around the pore formed due to the rapid cooling process (see Figure 1c, inset).³⁴ Figure 1d shows

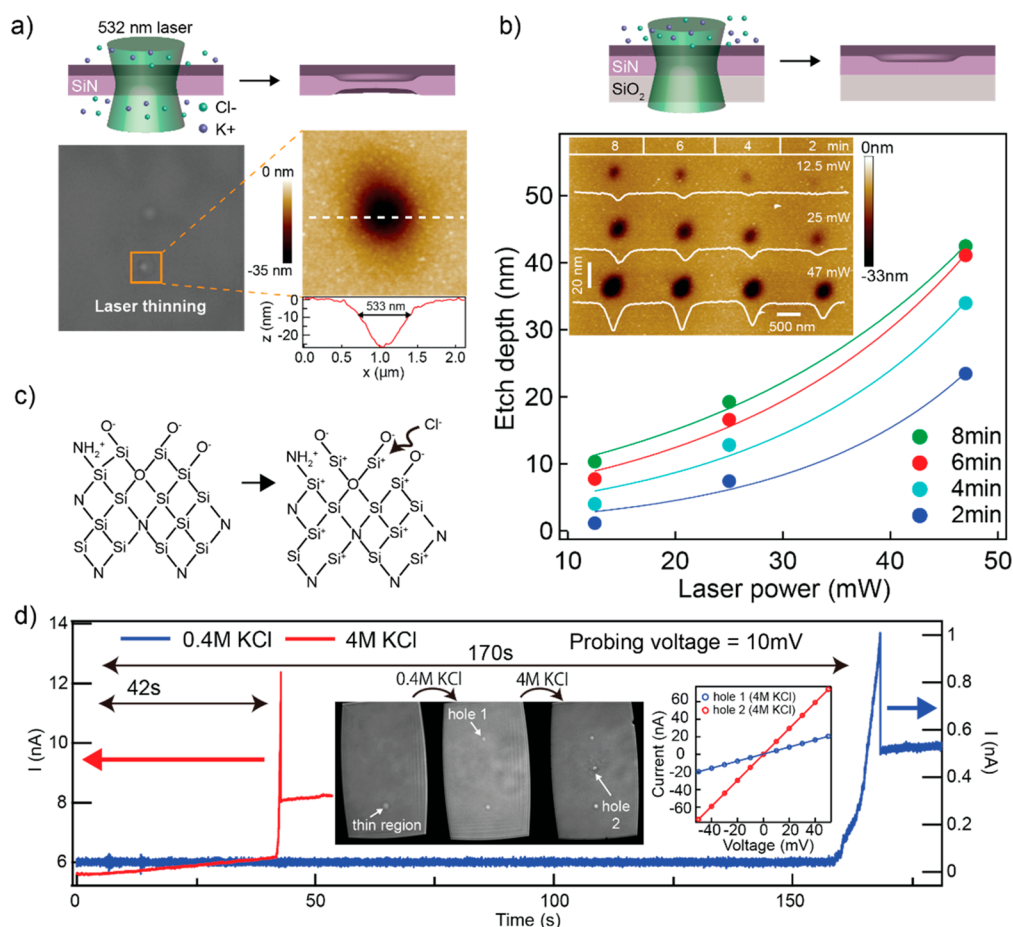


Figure 3. SiN_x dissolution kinetics and mechanism. (a) Schematic diagram of photochemical etching on freestanding SiN_x membrane. When collimated 532 nm laser was focused on a SiN_x freestanding membrane, locally photochemical etching starts at both sides of the membrane due to its exposure in aqueous chloride solutions. Optical image after photochemical etching with $P = 47$ mW (diameter of light spot: 710 nm) and $V = 1$ V for 3 min in 0.4 M KCl (etch width fwhm: 533 nm, maximum etch depth: 26.2 nm). (b) AFM-measured etch depth profiles laser at different laser powers and times for 75 nm-thick SiN_x supported by 2.5- μm -thick silicon oxide on silicon. Inset: AFM image of an etched array at indicated laser powers and times. The distance between each etched point was 3 μm . White lines are depth profiles measured across the center of the etch regions. (c) Proposed mechanism of photochemical SiN_x etching assisted by chloride ions. When Si-rich regions of SiN_x absorb the laser irradiation, the electron-poor photoactivated Si can attract Cl^- binding, promoting Si-Si bond breaks which lead to eventual oxidation. The resulting amorphous oxide is soluble at high temperatures, leading to thinning of the SiN_x membrane. (d) Continuous current trace of 75 nm-thick SiN_x membrane etching in 0.4 M KCl and 4 M KCl using a 10 mV probing voltage (laser power was 47 mW). When current threshold levels of 1 nA and 12 nA were reached for 0.4 and 4 M KCl, respectively, laser irradiation was shut off. Inset left: Optical images before laser-assisted SiN_x thinning, after first pore at 0.4 M KCl, and after second pore at 4 M KCl, respectively (left-to-right). Inset right: I - V curves after first and second pore formation, both recorded in 4 M KCl.

finite-element simulations of the 2D temperature profiles surrounding an air-suspended (top) and water-immersed (bottom) SiN_x membrane under 50 mW laser irradiation (COMSOL Multiphysics), revealing peak membrane temperatures of up to 1500 $^\circ\text{C}$ in air, in good agreement with SiN_x decomposition temperatures (~ 1530 $^\circ\text{C}$).³⁵ In contrast, peak temperatures found for the water-immersed SiN_x are much lower, due to the efficient heat removal by the surrounding water bath, which explains why rapid ablation was not observed when the SiN_x membrane was immersed in water.

However, when immersing the SiN_x in methanol, we found that we can consistently generate microbubbles by locally heating the SiN_x using 15 mW laser illumination, as shown in Figure 1e. The series of images, taken from a movie that depicts bubble formation (see Supporting Movie M2), show that a bubble forms immediately after switching the laser on (6–6.5 s), in which peak SiN_x temperatures reach 200 $^\circ\text{C}$ (see inset simulation), matching bubble nucleation temperatures on

SiN_x measured in methanol using on-membrane microheaters ($T_{\text{bubble}} = 155\text{--}240$ $^\circ\text{C}$).^{36,37} As soon as the laser is turned off, cooling causes the bubble to shrink and disappear within ~ 10 s due to instability. As further evidence of the impact of laser irradiation on the heating process, PL measurements reveal a lower emission yield as a function of laser power, which suggests a reduced emission yield, as previously measured for SiN_x with increasing temperatures (see Figure S1).^{32,33}

Controlled Photothermal Etching of SiN_x . The results thus far are a clear demonstration of the high temperatures reached when SiN_x is irradiated using a focused 532 nm laser at high power densities ($\sim 3 \times 10^7$ W/cm² at 50 mW laser power, assuming a $1/e^2$ beam diameter of 710 nm). To investigate the impact of the high-energy beam incident upon SiN_x on its integrity, in Figure 2a we show the ion current through a 6.4 nm diameter SiN_x nanopore fabricated using a TEM prior to the experiment (purple trace), when at $t = 5$ s, a 30 mW laser beam has been switched on. The instantaneous

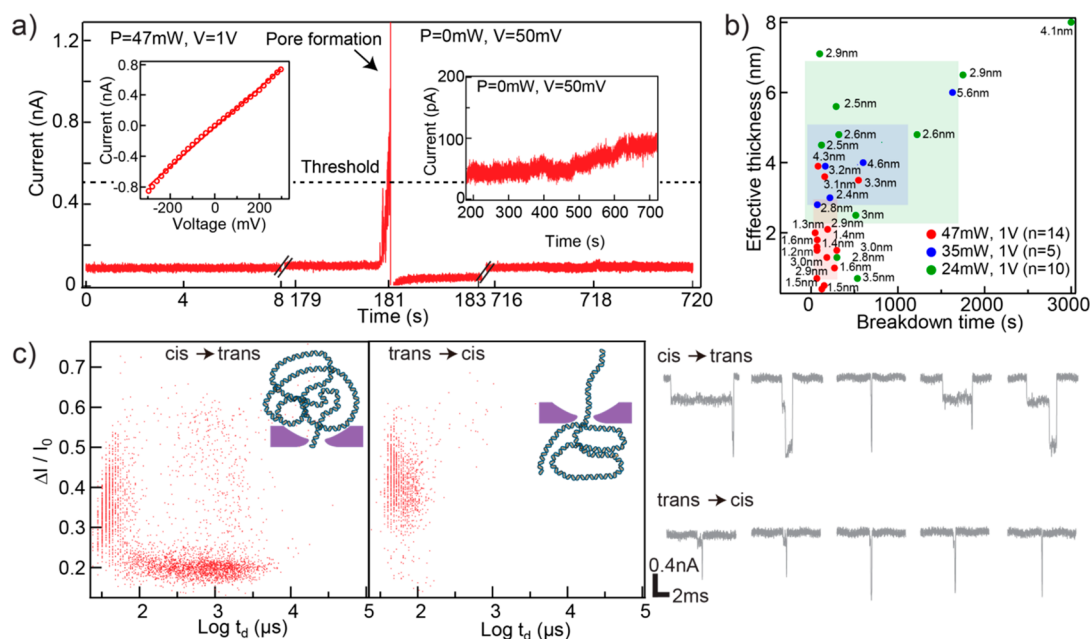


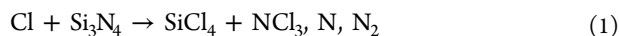
Figure 4. Laser-assisted dielectric breakdown for asymmetric nanopore fabrication. (a) Continuous current trace obtained during SiN_x laser-assisted dielectric breakdown (35 mW laser power, $V = 1$ V, laser turned on at 0 s). When pore formation is indicated by the current reaching 0.5 nA, the software turned off the laser, and a probing voltage of $V = 50$ mV was applied. Inset (left): $I-V$ curve of 2.4 nm diameter pore with 3 nm effective thickness formed using this method. Inset (right): 9 min continuous trace during pore expansion and stabilization at 50 mV probing voltage. (b) Scatter plot of pore thicknesses vs. breakdown times for 29 pores with three different laser powers used ($P = 47$ mW shown in red, $P = 35$ mW shown in blue, and $P = 24$ mW shown in green). Squares represent one standard deviation the parameters. Average breakdown times were 165 ± 67 s (47 mW), 536 ± 288 s (35 mW), and 814 ± 440 s (24 mW), and average effective respective thicknesses were 1.8 ± 1.1 nm, 3.9 ± 1.1 nm, and 4.6 ± 2.3 nm. (c) Typical $\Delta I/I_0$ vs. $\log t_d$ scatter plots obtained for 2.5 kbp DNA translocation dynamics through a 3.3 nm diameter pore with 2.8 nm effective thickness at 300 mV from *cis* (left) and *trans* (right) side. Right: Concatenated traces of DNA translocation events, low-pass-filtered at 10 kHz. DNA concentrations at *cis* and *trans* sides were 6 nM and 4 nM, respectively.

jump in ion current (see inset) is due to rapid heating caused by the laser, which results in a peak temperature at the pore of $T_p = 60$ °C. Pore temperature was calculated using the ion current enhancement profile, as described in our previous report.³⁸ However, following this current jump, we observed a gradual increasing of the ion current, and over a period of 10 min, the pore current approximately doubled. This ion current enhancement is likely due to a combination of SiN_x thinning and pore expansion, since both processes are consistent with stimulated dissolution of the SiN_x , as recently observed using a similar-wavelength (488 nm) and similar-intensity laser.^{21,38,39} When a bare 7.6 nm diameter SiN_x pore surface was passivated with a conformal layer of 1 nm-thick HfO_2 , a dielectric material, we found that HfO_2 greatly inhibits pore dissolution (blue trace). The current changes for the bare and HfO_2 -coated SiN_x pores are 5.0 and 0.6 pA/s, respectively. $I-V$ curves of both pores before and after the 10 min laser treatments, shown in the inset, highlight the photoreactivity of bare SiN_x .

To gain more insight into the factors that influence the observed SiN_x photothermal reactivity, we show in Figure 2b bright-field TEM images of a membrane which has been irradiated for 10 min at different locations using a 47 mW power ($T_p = 300$ °C), where prior to irradiation, the *cis* and *trans* fluids were replaced to expose the SiN_x membrane to either 0.4 M KCl, 0.4 M sodium acetate or pure water. Brightness in this TEM image corresponds to a higher transmitted electron dose through the membrane, which means that the SiN_x is thinnest in the case of chloride exposure. Based on these measurements, chloride is a more

effective promoter of SiN_x dissolution, whereas in acetate and pure water, SiN_x dissolution is minimal. This series of experiments was repeated with very similar results. Further, Figure 2c shows the impact of 8 h laser illumination at a power of 1.5 mW in 4 M KCl buffer. The slow etching of SiN_x under a weak laser illumination, in which the photothermal effect is negligible, emphasizes that the etching process is photo-thermally activated.^{32,33}

We further studied the dependence of light power and electrolyte strength on SiN_x dissolution kinetics by quantitative measurements using atomic force microscopy (AFM). Figure 3a shows the impact of a 3 min irradiation on a freestanding 75 nm-thick SiN_x membrane. AFM image of 47 mW laser illumination with $V = 1$ V for 3 min yields Gaussian distributed etch profiles²¹ (etch width fwhm: 533 nm, maximum etch depth: 26.2 nm). Notably, this etch profile matches the laser beam profile, as previously probed using nanopore tomography.⁴⁰ Further, we find that the etch rate depends nonlinearly on the laser power, which points to an activated chemical process as suggested by an Arrhenius equation, as shown in Figure 3b. Our combined observations suggest the following mechanism for the observed etching process: When silicon-rich SiN_x ($x \sim 1$) absorbs blue-green light, silicon bonds are activated by charge separation, which can likely lead to destabilization of Si-Si bonds in the Si-rich material.³³ We hypothesize that Cl^- can stabilize the transiently formed activated Si by forming transient Si-Cl bonds, which can explain Cl^- -promoted breakdown of activated Si-Si bonds, as shown in Figure 3c. We note here a known process in which chlorine plasma efficiently breaks down Si_3N_4 .⁴¹



Interestingly, photothermal heating has been shown to accelerate this process, especially at 300–500 °C.⁴² While the formed Si–Cl bond is unstable in the presence of water, Cl[−] can be rapidly displaced by water molecules leading to oxidation, in accordance with the observed reduction in PL upon irradiation.²¹ Dissolution of the resulting amorphous SiO₂ product can then be explained by the hot spot induced by the laser, since solubility of amorphous SiO₂ is enhanced greatly by temperature.⁴³ Further evidence of chloride-mediated SiN_x etching was obtained when we compared 75 nm SiN_x etching time in 0.4 and 4 M KCl on the same membrane. Figure 3d shows a current trace of a membrane under a focused 47 mW laser illumination at a low probing voltage of $V = 10$ mV, in which a hole was formed after 170 s when the electrolyte was 0.4 M KCl. In contrast, using 4 M KCl, a hole formed after 42 s, suggesting that an increased Cl[−] concentration is accelerating pore formation. Similar experiments using 0.04 M KCl resulted in ~ 3 times slower hole formation, consistent across three independent experimental sets. Finally, while small pH decreases (1–2 units) do result from heating tris buffer,⁴⁴ we note that etching was even faster at a higher pH, suggesting that slightly lower pH values cannot be responsible for this etching mechanism (0.1 M KOH, see SI Figure S2).

Laser-Assisted Dielectric Breakdown of Nanopores.

We find that laser-assisted SiN_x etching greatly facilitates the fabrication of ultrathin and ultrasmall nanopores using dielectric breakdown. Figure 4a shows a continuous current trace during laser-assisted dielectric breakdown ($V = 1$ V applied to the *cis* chamber, $P = 47$ mW). When the SiN_x membrane is sufficiently thin, breakdown can occur (<8 nm), and pore formation is marked by a sharp current rise, as seen at 180 s in the trace. Using software-based feedback, we stop the high-power laser illumination and reduce the voltage to 50 mV when the ion current reaches our specified threshold current (0.5 nA). After initial pore formation, we apply a weak voltage (50–100 mV) for up to 30 min to allow equilibration and stabilization of the pore current prior to adding biomolecules (see Figure 4a, inset). Since we used both laser heating and voltage, we assume that our dielectric breakdown process includes SiN_x thinning, thermal heating acceleration of defect production, and additional electric field by light.^{20,45–47} Pore size and its effective thickness are calculated using established methods that measure DNA blockades and DNA diameters (2.2 nm for dsDNA and 1.2 nm for ssDNA).^{48,49} Laser-induced breakdown allows us to fabricate a sub-5 nm diameter pore with thickness values that are well below 5 nm, as indicated by high blockade amplitudes we observe for translocations (continuous traces of DNA and tRNA translocations are shown in Figure S3). In Figure 4b we show pore thicknesses *vs* breakdown times and resulting pore diameters obtained using three different laser powers for a total of 29 pores made. The colored boxes represent one standard deviation in each parameter for the experiments conducted. We find that weak laser powers produce larger deviations in breakdown times and thicker pores, as compared with high laser powers, for which we routinely obtain pores with ~ 2 nm average thickness within 1–2 min of processing. Our results demonstrate the sophisticated control over laser power and voltage have over the delicate size and shape of nanopores.

Evidence for Asymmetric Nanopore Shape in Laser-Assisted Breakdown Pores.

One aspect of these pores fabricated using high laser powers is their shape, which is extremely difficult to image, yet for which DNA translocation data suggests a consistent pattern. In Figure 4c, we present 2.5 kbp DNA translocation dynamics through a pore ($d = 3.3$ nm, $t_{\text{eff}} = 2.8$ nm) made by our method as a function of the translocation direction. In the *cis*-to-*trans* direction, DNA translocation events have to clear two-blockade levels, a shallow one and a deep one, which corresponds to docking at the pore entrance due to its funnel-like shape, and translocation. Interestingly, this docking time is very long and almost always ends with translocation. In contrast, in the *trans*-to-*cis* direction we observe rapid deep events, suggesting that DNA docking times are much faster in this direction. A hypothesized mechanism for this result, which we observe consistently for pores generated using this method, is that the pore shape is asymmetric and funnel-like in shape. As the cartoons illustrate (see insets to Figure 4c, right), this asymmetric pore structure yields a pocket for DNA that results in longer docking times than when DNA approaches from the narrower opening. Further, we find different capture rates for DNA entering from either side, with rates of 3.19 ± 0.08 s^{−1} nM^{−1} for *cis*-to-*trans* direction and 1.05 ± 0.03 s^{−1} nM^{−1} for *trans*-to-*cis* direction. Both of these features, namely longer docking times and faster capture rates from *cis* entry into pore than from *trans* entry, were previously observed for ssDNA entry into the protein channel α -hemolysin.^{50,51} The asymmetric geometry is also suggested from the corresponding increase of effective thickness as pore size, as seen in Figure S4.

Ultrathin nanopores fabricated using laser-assisted dielectric breakdown can be used to differentiate two dsDNA lengths based on their dwell times in a DNA mixture.^{52,53} Figure 5a shows continuous current traces for a mixture of 250 bp (30 nM) and 2.5 kbp (3 nM) translocating through an ultrathin pore ($d = 2.7$ nm, $t_{\text{eff}} = 1.7$ nm) at 200, 250, and 300 mV. Scatter plots of $\Delta I/I_0$ *vs* $\log t_d$, shown in Figure 5b, reveal mean

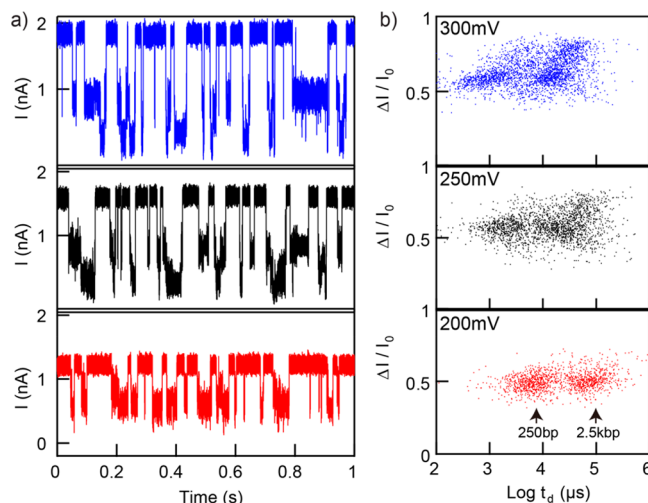


Figure 5. Discrimination of 250 bp and 2.5 kbp DNA. (a) Continuous 1 s trace excerpts at 200, 250, and 300 mV for a 2.7 nm pore with 1.7 nm effective thickness for a mixture of 250 bp (30 nM) and 2.5 kbp (3 nM) dsDNA added to the *cis* chamber. Traces were low-pass filtered at 20 kHz. (b) $\Delta I/I_0$ *vs* $\log t_d$ of mixture of 250 bp and 2.5 kbp at 200, 250, and 300 mV, showing an optimal resolution between the two lengths at 300 mV.

log t_d values for 250 bp/2.5 kbp of $3.80 \pm 0.01/4.79 \pm 0.01$, $3.36 \pm 0.03/4.47 \pm 0.02$, and $3.19 \pm 0.05/4.29 \pm 0.02$ μ s for 200, 250, and 300 mV, respectively (see also Figure S5). In this experiment, expansion of our pore was minimal despite the ultrathin SiN_x membrane, as shown by the 60 s current traces in Figure S6 which show a steady current level. Also, we find that as voltage increases, the 2.5 kbp dsDNA produces larger fractional blockades (but not the 250 bp DNA), attributed to interactions of the longer DNA coil with significant electric fields outside the pore.⁵³ We note that the long docking times observed with the larger 3.3 nm diameter pore in Figure 4 was not observed in this experiment, because the pore diameter is significantly smaller, which yields an electric field outside the pore that is too weak to trap DNA in the pore mouth.

DNA Homopolymer Differentiation Using Sub-2 nm-Thick Pores. Finally, we demonstrate the ability of an ultrathin sub-2 nm diameter pore ($d = 1.4$ nm, $t_{\text{eff}} = 1.8$ nm) to discriminate among two homopolymer types. Figure 6a schematically illustrates a vertically oriented membrane where a long template DNA (61-nucleotide) is inserted into the pore, and hybridized DNA oligomers (15 and 19 nucleotides) are sequentially unzipped by voltage-induced force applied to the DNA template (PAGE gel of hybridized product shown in Figure S7). In this experiment, we probe the current levels of poly(dA) and poly(dC) that are in the pore during the three-stage unzipping process. Under an applied voltage (200 mV), the poly(dC) tail of the template DNA enters the pore and resides there until the first duplex unzips, then the poly(dA) resides in the pore, and finally the poly(dC) resides in the pore. We find that events longer than 5 ms comprised 3.36% of the total events for the single-stranded 61-nucleotide DNA template, whereas for the hybridized sample, 20.3% of the events lasted longer than 5 ms, which we attribute to unzipping events (scatter plots and voltage effect on dsDNA unzipping are shown in Figures S8 and S9).⁵⁴ Within this long event population, in 18.6% of the events, we observed two distinct blockade levels, which we ascribe to the helix structure of poly(dC) and poly(dA) (Figure 6b). As with α -hemolysin experiments, the 1.3 nm-wide poly(C) helical secondary structure can be accommodated in 1.4 nm pore, while the 2.1 nm-wide poly(A) helix is too large to fit inside the narrow pore,⁵⁵ resulting in a shallower blockade current for poly(dA). Figure 6c shows current blockade levels of poly(dC) and poly(dA) and its difference from the same pore (all current traces in Figure 6c are shown in Figure S10). The mean ΔI difference between dA and dC (Figure 6d) in all these events is 16.9 ± 1.4 pA, in good agreement with previous α -hemolysin and MspA experiments.^{55–57} Although nucleotide resolution using a solid-state nanopore was previously demonstrated by homopolymer discrimination,^{58–60} our results show that ultrathin solid-state nanopore has the sensitivity to discriminate both types of polymers within a single molecular chain.

CONCLUSION

In conclusion, we have investigated in detail the mechanism of laser-assisted SiN_x etching and demonstrated a method for fabricating ultrasmall and ultrathin nanopores that are useful for biomolecular analysis. We first showed the thermal impact of laser irradiation on SiN_x, which causes rapid hole formation by laser-induced thermal ablation in air and methanol microbubble nucleation at the SiN_x/methanol interface, both processes induced by ~ 1500 °C and ~ 200 °C SiN_x surface temperatures, respectively. Next, we showed that HfO₂ coating

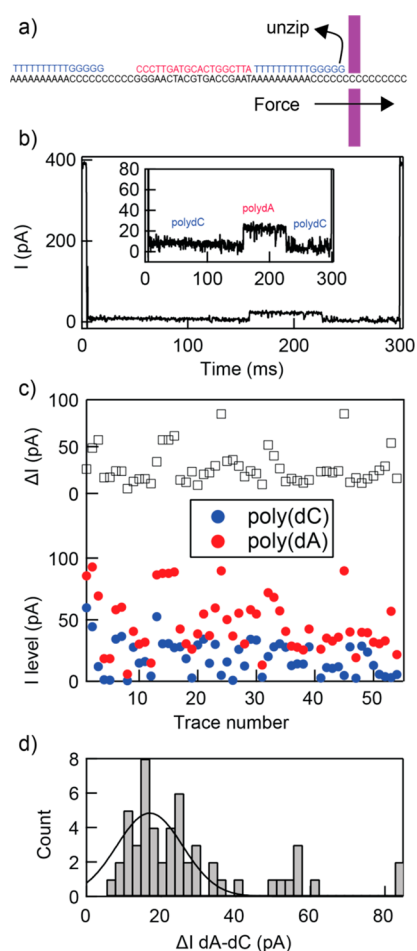


Figure 6. Current discrimination of dC and dA homopolymers using an ultrathin laser-assisted breakdown pore. (a) Schematic diagram of sequentially unzipping dsDNA to expose a predetermined temporal sequence of homopolymers to the pore. During unzipping DNA duplex, either a poly(dC) or a poly(dA) portion of the ssDNA template resides inside the pore, allowing residual ion currents to be probed. Designed DNA is in the probing order of poly(dC), poly(dA), and poly(dC). (b) Current trace of DNA unzipping in a 1.4 nm diameter pore with 1.8 nm effective thickness at 200 mV (trace was low-pass-filtered at 1 kHz). The expanded trace with poly(dC) and poly(dA) labels is shown in the inset. (c) I levels of poly(dC) (blue markers) and poly(dA) (red markers) and ΔI dA-dC (black squares). Current levels were obtained by double Gaussian fits to the current histograms of each event. (d) Histogram of differential ΔI dA-dC with the Gaussian fit. Mean ΔI current difference between dA and dC levels was 16.9 ± 1.4 pA.

of a SiN_x surface efficiently inhibited light-induced etching of a SiN_x pore using electrical measurements. While in fluid, temperatures are relatively low and cannot account for SiN_x ablation, we find that a photochemical oxidation process, potentially mediated by chloride ions and alkaline conditions, coupled to thermally induced dissolution of the resulting amorphous oxide, results in a controlled etching process that thins SiN_x at controlled rates that can easily be ~ 0.2 nm/s (Figure S11). Coupling this process to dielectric breakdown results in a procedure using fairly common setups for ultrathin and ultrasmall nanopores (< 2 nm in diameter and thickness), which can discriminate DNA length as well as sense DNA homopolymer sequence identification. Our approach provides

a controlled process for nanopores that can exceed biological nanopores in terms of their sharp geometry, approaching 2D materials thickness.

METHODS

Nanopore Experiments and Molecules Tested. In all experiments, $5 \times 5 \text{ mm}^2$ Si chips that have $\sim 75 \text{ nm}$ -thick freestanding SiN_x membranes with $20\text{--}50 \mu\text{m}$ window sizes were used. Prior to SiN_x deposition and membrane fabrication, a $2.5 \mu\text{m}$ -thick thermal SiO_2 layer has been grown on both sides of the wafer, in order to reduce capacitive noise. Each membrane had a single $1\text{--}3 \mu\text{m}$ -wide circular region which had a reduced thickness, fabricated by aligning a hole pattern on the membrane side back-aligned to the window positions. Following exposure of the hole array, thin regions were generated using reactive ion etching.

Nanopores for the data in Figure 2 were fabricated using transmission electron microscopy (JEOL 2010F), and HfO_2 coating was carried out by depositing 1 nm HfO_2 layer on 8 nm pore following treatment using hot piranha solution (1:2 mixture of H_2O_2 and H_2SO_4) for $\sim 15 \text{ min}$. HfO_2 -coated SiN_x pores in experiments were cleaned by a 30 s O_2 plasma treatment, followed by a 3 min immersion in hot piranha. Cleaned chips were mounted in a custom PTFE cell which was filled with electrolyte buffer on both sides, each equipped with an Ag/AgCl electrode connected to an Axopatch 200B. Buffers used in this work were 0.4 and 4 M KCl with 10 mM Tris, and 1 mM EDTA, pH 7.9, except for the 0.04 M buffer, which was a 10-fold diluted 0.4 M KCl buffer as above, 0.4 M sodium acetate self-buffered to pH 5.1, and unbuffered water at pH 7.4. The leakage current before laser SiN_x thinning was low ($\sim 200 \text{ pA}$ at 1 V) for all pore fabrications. The starting material for all pore fabrication experiments that use a combination of dielectric breakdown and laser was a 75 nm -thick SiN_x membrane. All pore sizes ($d < 5 \text{ nm}$) and effective thicknesses were calculated using equations developed in prior work that takes into account access resistance.⁴⁸ Analysis of current blockades and dwell times was performed using custom Python software, developed in the Wanunu Lab (<https://github.com/rhenley/Pyth-Ion/>). Tested chip information is summarized in Table S1 and S2.

DNA oligonucleotides were purchased from Integrated DNA Technologies, Inc. and used without further purifications. The DNA sequences are

61-nucleotide template: AAAAAAAAAACCCCCCCCCCTT-GATGCACTGGCTTAAAAAAAAACCCCCCCCCCCCCC

19-nucleotide oligomer: TAAGCCAGTGCATCAAGGG

15-nucleotide oligomer: TTTTTTTTTTGGGGG

In order to hybridize the oligomers for the data in Figure 6, the mixture of three DNA samples (concentrations adjusted at $6 \mu\text{M}$, $6 \mu\text{M}$, and $12 \mu\text{M}$, respectively) was incubated in nuclease-free water at $90 \text{ }^\circ\text{C}$ for 10 min and cooled down to room temperature. Hybridization proceeded with $\sim 70\%$ efficiency, as confirmed by PAGE gel electrophoresis (Figure S7).

Finite-Element Simulations. For membrane temperature estimation, we used COMSOL Multiphysics software. A 75 nm -thick SiN_x membrane surrounded by a fluid (either water, methanol, or air) was used for the calculation model. The heating source, which takes into account the material properties of SiN_x and laser power, was placed at the bottom of the membrane, and the theoretical model used here was the first law of thermodynamics. More details about these simulations are provided in our previous work.³⁸

ASSOCIATED CONTENT

Supporting Information

The Supporting Information is available free of charge on the ACS Publications website at DOI: 10.1021/acsnano.8b06805.

PL kinetics of SiN_x membrane; SiN_x etching in 0.1 KOH ; current trace or analyzed data of DNA, RNA, mixture of 250 bp and 2.5 kbp , 61-nucleotide ssDNA

and duplex DNA samples; PAGE gel image; summary of test chips for SiN_x etching and pore formation (PDF)
Movie M1: 75 nm SiN ablation in air (AVI)
Movie M2: Bubble formation in methanol (AVI)

AUTHOR INFORMATION

Corresponding Author

*E-mail: wanunu@neu.edu.

ORCID

Qing Zhao: 0000-0003-3374-6901

Meni Wanunu: 0000-0002-9837-0004

Author Contributions

H.Y. and M.W. conceived all experiments. H.Y. performed all experiments. R.H. designed the HfO_2 -coated SiN_x etching test. The manuscript was written by H.Y. and M.W., and all authors commented on it.

Notes

The authors declare no competing financial interest.

ACKNOWLEDGMENTS

This work was supported by funding from the National Science Foundation (EFMA-1542707, M.W.). H.Y. is a recipient of JSPS Postdoctoral Fellowships for Research Abroad. We acknowledge chemical mechanism discussions with Dr. Ovadia Abed, assistance with gel electrophoresis from Xinqi Kang, and freestanding SiN_x membrane chip fabrication by Dr. Mohammad Amin Alibakhshi.

REFERENCES

- (1) Storm, A. J.; Chen, J. H.; Ling, X. S.; Zandbergen, H. W.; Dekker, C. Fabrication of Solid-state Nanopores with Single-nanometre Precision. *Nat. Mater.* **2003**, *2*, 537.
- (2) Kim, M. J.; Wanunu, M.; Bell, D. C.; Meller, A. Rapid Fabrication of Uniformly Sized Nanopores and Nanopore Arrays for Parallel DNA Analysis. *Adv. Mater.* **2006**, *18*, 3149–3153.
- (3) Rodríguez-Manzo, J. A.; Puster, M.; Nicolai, A.; Meunier, V.; Drndić, M. DNA Translocation in Nanometer Thick Silicon Nanopores. *ACS Nano* **2015**, *9*, 6555–6564.
- (4) Li, J.; Stein, D.; McMullan, C.; Branton, D.; Aziz, M. J.; Golovchenko, J. A. Ion-beam Sculpting at Nanometre Length Scales. *Nature* **2001**, *412*, 166.
- (5) Yang, J.; Ferranti, D. C.; Stern, L. A.; Sanford, C. A.; Huang, J.; Ren, Z.; Qin, L.-C.; Hall, A. R. Rapid and Precise Scanning Helium Ion Microscope Milling of Solid-state Nanopores for Biomolecule Detection. *Nanotechnology* **2011**, *22*, 285310.
- (6) Schneider, G. F.; Kowalczyk, S. W.; Calado, V. E.; Pandraud, G.; Zandbergen, H. W.; Vandersypen, L. M. K.; Dekker, C. DNA Translocation through Graphene Nanopores. *Nano Lett.* **2010**, *10*, 3163–3167.
- (7) Merchant, C. A.; Healy, K.; Wanunu, M.; Ray, V.; Peterman, N.; Bartel, J.; Fischbein, M. D.; Venta, K.; Luo, Z.; Johnson, A. T. C.; Drndić, M. DNA Translocation through Graphene Nanopores. *Nano Lett.* **2010**, *10*, 2915–2921.
- (8) Liu, K.; Feng, J.; Kis, A.; Radenovic, A. Atomically Thin Molybdenum Disulfide Nanopores with High Sensitivity for DNA Translocation. *ACS Nano* **2014**, *8*, 2504–2511.
- (9) Feng, J.; Liu, K.; Bulushev, R. D.; Khlybov, S.; Dumcenco, D.; Kis, A.; Radenovic, A. Identification of Single Nucleotides in MoS_2 Nanopores. *Nat. Nanotechnol.* **2015**, *10*, 1070.
- (10) Waduge, P.; Bilgin, I.; Larkin, J.; Henley, R. Y.; Goodfellow, K.; Graham, A. C.; Bell, D. C.; Vamivakas, N.; Kar, S.; Wanunu, M. Direct and Scalable Deposition of Atomically Thin Low-Noise MoS_2 Membranes on Apertures. *ACS Nano* **2015**, *9*, 7352–7359.
- (11) Danda, G.; Masih Das, P.; Chou, Y.-C.; Mlack, J. T.; Parkin, W. M.; Naylor, C. H.; Fujisawa, K.; Zhang, T.; Fulton, L. B.; Terrones,

- M.; Johnson, A. T. C.; Drndić, M. Monolayer WS₂ Nanopores for DNA Translocation with Light-Adjustable Sizes. *ACS Nano* **2017**, *11*, 1937–1945.
- (12) Briggs, K.; Kwok, H.; Tabard-Cossa, V. Automated Fabrication of 2-nm Solid-State Nanopores for Nucleic Acid Analysis. *Small* **2014**, *10*, 2077–2086.
- (13) Kwok, H.; Briggs, K.; Tabard-Cossa, V. Nanopore Fabrication by Controlled Dielectric Breakdown. *PLoS One* **2014**, *9*, No. e92880.
- (14) Briggs, K.; Charron, M.; Kwok, H.; Le, T.; Chahal, S.; Bustamante, J.; Waugh, M.; Tabard-Cossa, V. Kinetics of Nanopore Fabrication during Controlled Breakdown of Dielectric Membranes in Solution. *Nanotechnology* **2015**, *26*, 084004.
- (15) Carlsen, A. T.; Briggs, K.; Hall, A. R.; Tabard-Cossa, V. Solid-state Nanopore Localization by Controlled Breakdown of Selectively Thinned Membranes. *Nanotechnology* **2017**, *28*, 085304.
- (16) Kuan, A. T.; Lu, B.; Xie, P.; Szalay, T.; Golovchenko, J. A. Electrical Pulse Fabrication of Graphene Nanopores in Electrolyte Solution. *Appl. Phys. Lett.* **2015**, *106*, 203109.
- (17) Feng, J.; Liu, K.; Graf, M.; Lihter, M.; Bulushev, R. D.; Dumcenco, D.; Alexander, D. T. L.; Krasnozhan, D.; Vuletic, T.; Kis, A.; Radenovic, A. Electrochemical Reaction in Single Layer MoS₂: Nanopores Opened Atom by Atom. *Nano Lett.* **2015**, *15*, 3431–3438.
- (18) Arcadia, C. E.; Reyes, C. C.; Rosenstein, J. K. *In Situ* Nanopore Fabrication and Single-Molecule Sensing with Microscale Liquid Contacts. *ACS Nano* **2017**, *11*, 4907–4915.
- (19) Yanagi, I.; Akahori, R.; Hatano, T.; Takeda, K.-i. Fabricating Nanopores with Diameters of Sub-1 to 3 nm using Multilevel Pulse-voltage Injection. *Sci. Rep.* **2015**, *4*, 5000.
- (20) Pud, S.; Verschuere, D.; Vukovic, N.; Plesa, C.; Jonsson, M. P.; Dekker, C. Self-Aligned Plasmonic Nanopores by Optically Controlled Dielectric Breakdown. *Nano Lett.* **2015**, *15*, 7112–7117.
- (21) Gilboa, T.; Zrehen, A.; Girsault, A.; Meller, A. Optically-Monitored Nanopore Fabrication Using a Focused Laser Beam. *Sci. Rep.* **2018**, *8*, 9765.
- (22) Yuan, Y.; Li, G.; Zaribafzadeh, H.; de la Mata, M.; Castro-Hartmann, P.; Zhang, Q.; Arbiol, J.; Xiong, Q. Sub-20 nm Nanopores Sculptured by a Single Nanosecond Laser Pulse. *Arxiv* 2018, <https://arxiv.org/abs/1806.08172>.
- (23) Ying, C.; Houghtaling, J.; Eggenberger, O. M.; Guha, A.; Nirmalraj, P.; Awasthi, S.; Tian, J.; Mayer, M. Formation of Single Nanopores with Diameters of 20–50 nm in Silicon Nitride Membranes Using Laser-Assisted Controlled Breakdown. *ACS Nano* **2018**, *12*, 11458–11470.
- (24) Zrehen, A.; Gilboa, T.; Meller, A. Real-time Visualization and Sub-diffraction Limit Localization of Nanometer-scale Pore Formation by Dielectric Breakdown. *Nanoscale* **2017**, *9*, 16437–16445.
- (25) Wang, Y.; Ying, C.; Zhou, W.; de Vreede, L.; Liu, Z.; Tian, J. Fabrication of Multiple Nanopores in a SiN_x Membrane via Controlled Breakdown. *Sci. Rep.* **2018**, *8*, 1234.
- (26) Uram, J. D.; Ke, K.; Hunt, A. J.; Mayer, M. Label-Free Affinity Assays by Rapid Detection of Immune Complexes in Submicrometer Pores. *Angew. Chem., Int. Ed.* **2006**, *45*, 2281–2285.
- (27) Joglekar, A. P.; Liu, H.; Spooner, G. J.; Meyhöfer, E.; Mourou, G.; Hunt, A. J. A Study of the Deterministic Character of Optical Damage by Femtosecond Laser Pulses and Applications to Nanomachining. *Appl. Phys. B: Lasers Opt.* **2003**, *77*, 25–30.
- (28) Joglekar, A. P.; Liu, H.-h.; Meyhöfer, E.; Mourou, G.; Hunt, A. J. Optics at Critical Intensity: Applications to Nanomorphing. *Proc. Natl. Acad. Sci. U. S. A.* **2004**, *101*, 5856–5861.
- (29) Danda, G.; Masih Das, P.; Drndić, M. Laser-induced Fabrication of Nanoporous Monolayer WS₂ Membranes. *2D Mater.* **2018**, *5*, 035011.
- (30) Xanthakis, J. P.; Papadopoulos, S.; Mason, P. R. The Electronic Structure of SiN_x: the Valence Band DOS and Band Gaps. *J. Phys. C: Solid State Phys.* **1988**, *21*, L555.
- (31) ACS NanoPark, J.; Heo, S.; Chung, J.-G.; Kim, H.; Lee, H.; Kim, K.; Park, G.-S. Bandgap Measurement of Thin Dielectric Films using Monochromated STEM-EELS. *Ultramicroscopy* **2009**, *109*, 1183–1188.
- (32) Deshpande, S. V.; Gulari, E.; Brown, S. W.; Rand, S. C. Optical Properties of Silicon Nitride Films Deposited by Hot Filament Chemical Vapor Deposition. *J. Appl. Phys.* **1995**, *77*, 6534–6541.
- (33) Giorgis, F.; Vinegoni, C.; Pavesi, L. Optical Absorption and Photoluminescence Properties of a-Si_{1-x}N_x: H Films Deposited by Plasma-enhanced CVD. *Phys. Rev. B: Condens. Matter Mater. Phys.* **2000**, *61*, 4693–4698.
- (34) Samant, A. N.; Dahotre, N. B. Laser Machining of Structural Ceramics—A Review. *J. Eur. Ceram. Soc.* **2009**, *29*, 969–993.
- (35) Atanasov, P. A.; Eugenieva, E. D.; Nedialkov, N. N. Laser Drilling of Silicon Nitride and Alumina Ceramics: A Numerical and Experimental Study. *J. Appl. Phys.* **2001**, *89*, 2013–2016.
- (36) Ching, E. J.; Thomas Avedisian, C.; Cavicchi, R. C.; Chung, D. H.; Rah, K. J.; Carrier, M. J. Rapid Evaporation at the Superheat Limit of Methanol, Ethanol, Butanol and n-Heptane on Platinum Films supported by Low-stress SiN Membranes. *Int. J. Heat Mass Transfer* **2016**, *101*, 707–718.
- (37) Poling, B. E.; Prausnitz, J. M.; O'Connell, J. P. *Properties of Gases and Liquids*, 4th ed.; McGraw-Hill: New York, 1987.
- (38) Yamazaki, H.; Hu, R.; Henley, R. Y.; Halman, J.; Afonin, K. A.; Yu, D.; Zhao, Q.; Wanunu, M. Label-Free Single-Molecule Thermoscopy Using a Laser-Heated Nanopore. *Nano Lett.* **2017**, *17*, 7067–7074.
- (39) Nicoli, F.; Verschuere, D.; Klein, M.; Dekker, C.; Jonsson, M. P. DNA Translocations through Solid-State Plasmonic Nanopores. *Nano Lett.* **2014**, *14*, 6917–6925.
- (40) Keyser, U. F.; Krapf, D.; Koeleman, B. N.; Smeets, R. M. M.; Dekker, N. H.; Dekker, C. Nanopore Tomography of a Laser Focus. *Nano Lett.* **2005**, *5*, 2253–2256.
- (41) Pant, B. D.; Tandon, U. S. Etching of Silicon Nitride in CCl₂F₂, CHF₃, SiF₄, and SF₆ Reactive Plasma: A Comparative Study. *Plasma Chem. Plasma Process.* **1999**, *19*, 545–563.
- (42) Staffa, J.; Hwang, D.; Luther, B.; Ruzyllo, J.; Grant, R. Temperature Dependence of the Etch Rate and Selectivity of Silicon Nitride over Silicon Dioxide in Remote Plasma NF₃/Cl₂. *Appl. Phys. Lett.* **1995**, *67*, 1902–1904.
- (43) Fournier, R. O.; Rowe, J. J. The Solubility of Amorphous Silica at High Temperatures and High Pressures. *Am. Mineral.* **1977**, *62*, 1052–1056.
- (44) Reineke, K.; Mathys, A.; Knorr, D. Shift of pH-Value During Thermal Treatments in Buffer Solutions and Selected Foods. *Int. J. Food Prop.* **2011**, *14*, 870–881.
- (45) Rothenmund, W.; Fritzsche, C. R. Dielectric Breakdown of Reactively Sputtered Silicon Nitride. *Thin Solid Films* **1973**, *15*, 199–205.
- (46) Lombardo, S.; Stathis, J. H.; Linder, B. P.; Pey, K. L.; Palumbo, F.; Tung, C. H. Dielectric Breakdown Mechanisms in Gate Oxides. *J. Appl. Phys.* **2005**, *98*, 121301.
- (47) McPherson, J. W.; Mogul, H. C. Underlying Physics of the Thermochemical E Model in Describing Low-field Time-dependent Dielectric Breakdown in SiO₂ Thin Films. *J. Appl. Phys.* **1998**, *84*, 1513–1523.
- (48) Wanunu, M.; Dadosh, T.; Ray, V.; Jin, J.; McReynolds, L.; Drndić, M. Rapid Electronic Detection of Probe-specific microRNAs using Thin Nanopore Sensors. *Nat. Nanotechnol.* **2010**, *5*, 807.
- (49) Kowalczyk, S. W.; Grosberg, A. Y.; Rabin, Y.; Dekker, C. Modeling the Conductance and DNA Blockade of Solid-state Nanopores. *Nanotechnology* **2011**, *22*, 315101.
- (50) Henrickson, S. E.; Misakian, M.; Robertson, B.; Kasianowicz, J. J. Driven DNA Transport into an Asymmetric Nanometer-Scale Pore. *Phys. Rev. Lett.* **2000**, *85*, 3057–3060.
- (51) Bell, N. A. W.; Chen, K.; Ghosal, S.; Ricci, M.; Keyser, U. F. Asymmetric Dynamics of DNA Entering and Exiting a Strongly Confining Nanopore. *Nat. Commun.* **2017**, *8*, 380.
- (52) Fologea, D.; Brandin, E.; Uplinger, J.; Branton, D.; Li, J. DNA Conformation and Base Number Simultaneously Determined in a Nanopore. *Electrophoresis* **2007**, *28*, 3186–3192.

(53) Carson, S.; Wilson, J.; Aksimentiev, A.; Wanunu, M. Smooth DNA Transport through a Narrowed Pore Geometry. *Biophys. J.* **2014**, *107*, 2381–2393.

(54) Lin, Y.; Shi, X.; Liu, S.-C.; Ying, Y.-L.; Li, Q.; Gao, R.; Fathi, F.; Long, Y.-T.; Tian, H. Characterization of DNA Dduplex Unzipping through a Sub-2 nm Solid-state Nanopore. *Chem. Commun.* **2017**, *53*, 3539–3542.

(55) Akeson, M.; Branton, D.; Kasianowicz, J. J.; Brandin, E.; Deamer, D. W. Microsecond Time-Scale Discrimination Among Polycytidylic Acid, Polyadenylic Acid, and Polyuridylic Acid as Homopolymers or as Segments Within Single RNA Molecules. *Biophys. J.* **1999**, *77*, 3227–3233.

(56) Derrington, I. M.; Butler, T. Z.; Collins, M. D.; Manrao, E.; Pavlenok, M.; Niederweis, M.; Gundlach, J. H. Nanopore DNA Sequencing with MspA. *Proc. Natl. Acad. Sci. U. S. A.* **2010**, *107*, 16060–16065.

(57) Meller, A.; Nivon, L.; Brandin, E.; Golovchenko, J.; Branton, D. Rapid Nanopore Discrimination between Single Polynucleotide Molecules. *Proc. Natl. Acad. Sci. U. S. A.* **2000**, *97*, 1079–1084.

(58) Venta, K.; Shemer, G.; Puster, M.; Rodríguez-Manzo, J. A.; Balan, A.; Rosenstein, J. K.; Shepard, K.; Drndić, M. Differentiation of Short, Single-Stranded DNA Homopolymers in Solid-State Nanopores. *ACS Nano* **2013**, *7*, 4629–4636.

(59) Akahori, R.; Yanagi, I.; Goto, Y.; Harada, K.; Yokoi, T.; Takeda, K.-i. Discrimination of Three Types of Homopolymers in Single-stranded DNA with Solid-state Nanopores through External Control of the DNA Motion. *Sci. Rep.* **2017**, *7*, 9073.

(60) Lee, M.-H.; Kumar, A.; Park, K.-B.; Cho, S.-Y.; Kim, H.-M.; Lim, M.-C.; Kim, Y.-R.; Kim, K.-B. A Low-Noise Solid-State Nanopore Platform Based on a Highly Insulating Substrate. *Sci. Rep.* **2015**, *4*, 7448.